EUROPEAN FUSION DEVELOPMENT AGREEMENT

EFDA–JET–PR(03)21

M.J. Mantsinen, M.-L. Mayoral, D. Van Eester, B. Alper, R. Barnsley, P. Beaumont, J. Bucalossi, I. Coffey, S. Conroy, M. de Baar, P. de Vries, K. Erents, A. Figueiredo, A. Gondhalekar, C. Gowers, T. Hellsten, E. Joffrin, V. Kiptily, P.U. Lamalle, K. Lawson, A. Lyssoivan, J. Mailloux, P. Mantica, F. Meo, F. Milani, I. Monakhov, A. Murari, F. Nguyen, J.-M. Noterdaeme, J. Ongena, Yu. Petrov, E. Rachlew, V. Riccardo, E. Righi, F. Rimini, M. Stamp, A.A. Tuccillo, K.-D. Zastrow, M. Zerbini and JET EFDA contributors*

Localised Bulk Electron Heating with ICRF Mode Conversion in the JET Tokamak

Localised Bulk Electron Heating with ICRF Mode Conversion in the JET Tokamak

M.J. Mantsinen, M.-L. Mayoral, D. Van Eester, B. Alper, R. Barnsley, P. Beaumont, J. Bucalossi, I. Coffey, S. Conroy, M. de Baar, P. de Vries, K. Erents, A. Figueiredo, A. Gondhalekar, C. Gowers, T.Hellsten, E. Joffrin, V. Kiptily, P.U. Lamalle, K. Lawson, A. Lyssoivan, J. Mailloux, P. Mantica, F. Meo, F. Milani, I. Monakhov, A.Murari, F. Nguyen, J.-M. Noterdaeme, J. Ongena, Yu. Petrov, E. Rachlew, V. Riccardo, E. Righi, F. Rimini, M. Stamp, A.A. Tuccillo, K.-D. Zastrow, M. Zerbini and JET EFDA contributors*

[1]*Helsinki University of Technology, Association Euratom-Tekes, Finland*
[2]*Association Euratom-UKAEA, Culham Science Centre, Abingdon, United Kingdom*
[3]*LPP-ERM/KMS, Association Euratom-Belgian State, TEC, Brussels, Belgium*
[4]*Association EURATOM-CEA, CEA-Cadarache, Saint-Paul-Lez Durance, France*
[5]*Euratom-VR Association, Swedish Research Council, Stockholm, Sweden*
[6]*FOM-Rijnhuizen, Ass. Euratom-FOM, TEC, Nieuwegein, The Netherlands*
[7]*Associação EURATOM-IST, Centro de Fus,,o Nuclear, Lisboa, Portugal*
[8]*EFDA-JET CSU, Culham Science Centre, Abingdon, United Kingdom*
[9]*Istituto di Fisica del Plasma, EURATOM-ENEA-CNR Association, Milan, Italy*
[10]*Max-Planck IPP-EURATOM Assoziation, Garching, Germany*
[11]*Consorzio RFX, Associazione Euratom-Enea sulla Fusione, Padova, Italy*
[12]*Gent University, Belgium*
[13]*Prairie View A&M University, Prairie View, USA*
[14]*EFDA-CSU, Garching, Germany*
[15]*Present address: European Commission, Brussels, Belgium*
[16]*Associazione EURATOM-ENEA sulla Fusione, CR Frascati, Rome, Italy*
** See annex of J. Pamela et al, "Overview of Recent JET Results and Future Perspectives", Fusion Energy 2000 (Proc. 18th Int. Conf. Sorrento, 2000), IAEA, Vienna (2001).*

Preprint of Paper to be submitted for publication in
Nuclear Fusion

ABSTRACT

ICRF mode conversion has been developed for localised on-axis and off-axis bulk electron heating on the JET tokamak. The fast magnetosonic waves launched from the low-field-side ICRF antennas are mode-converted to short-wavelength waves on the high-field side of the ^{3}He ion cyclotron resonance layer in D and ^{4}He plasmas and subsequently damped on the bulk electrons. The resulting electron power deposition, measured using ICRF power modulation, is narrow with a typical full width at half maximum of ≈30 cm (i.e. about 30% of the minor radius) and comprises at least up to 80% of the applied ICRF power. The ICRF mode conversion power deposition has been kept constant using ^{3}He bleed throughout the ICRF phase with a typical duration of 4-6s, i.e. 15-40 energy confinement times. Using waves propagating in the counter-current direction minimises competing ion damping in the presence of co-injected deuterium beam ions.

1. INTRODUCTION

On the JET tokamak, ICRF heating is a well-established heating method used in all main plasma regimes. In particular, heating at the fundamental or harmonic ion cyclotron resonance frequencies [1] has been successfully applied to obtain bulk ion and/or electron heating in a variety of experimental conditions. While these schemes allow for the control of the heating location by changing the resonance position, the resulting power deposition profiles are typically rather broad due to the Doppler broadening of the ion cyclotron resonance layer, the spread of the wave field along the resonance layer and the finite orbit widths of ICRF resonant fast ions. The heating takes place on the rather long time-scale of fast ion collisional slowing down (typically of the order of 1s for electron heating in JET experiments), which is not optimal when a fast response is required. Indeed, there are situations where bulk plasma heating is required with good controllability both with respect to its location and response to the switch-on and switch-off of the ICRF power. The long slowing down time of fast ions also increases the plasma pressure by increasing the pressure of the fast ions. With fast wave Transit Time Magnetic Pumping (TTMP) and Electron Landau Damping (ELD), a better time response on the time scale of electron-electron collisions (i.e. of the order of milliseconds) has been achieved [2, 3], but the possibilities to control the heating power localisation are limited.

This paper reports the development of ICRF Mode Conversion (MC) on JET for localised electron heating that can be controlled both in space and time. This scheme is attractive for profile and MHD activity control and it has been instrumental in, for example, studying plasma heat transport on JET [4]. It has the advantage of minimising the population of fast ions, which could be useful e.g. for steady-state advanced mode operation at low current (which could have poor fast ion confinement on the present-day tokamaks) or for modifying the electron to ion temperature ratio without introducing significant populations of ICRF-accelerated fast ions. The scheme is based on mode conversion of the launched fast magnetosonic wave to short-wavelength waves in a plasma with two main ion species with comparable concentrations, such as Tritium-Deuterium (D-T) plasma in a reactor. The mode-converted waves damp predominantly on electrons in the vicinity of the mode conversion layer, the

position of which can be controlled by changing the magnetic field, wave frequency or ion species mixture.

Previously, significant bulk electron heating due to ICRF MC, involving up to 90% of coupled ICRF power, has been reported in experiments on several smaller tokamaks [5-13]. While discharges have been carried out on JET in the conditions where ICRF MC has been expected to take place [14,15], a systematic investigation involving detailed measurements of direct electron power deposition with ICRF MC on JET has been lacking. Peaking of electron power deposition attributable to ICRF MC on JET has been reported earlier [16, 2], but with a relatively small fraction (<20%) of the total ICRF power deposited on electrons via mode-converted waves. In order to have confidence in the use of ICRF MC in next-step tokamaks, it is important to investigate whether high-efficiency localised on-axis and off-axis electron heating observed on other tokamaks can be reproduced on larger present-day tokamaks such as JET (major radius $R_0 \approx 3$ m, equatorial minor radius $a \approx 0.95$ m). In addition to localised electron heating, several other reactor-relevant applications for ICRF MC have been proposed. These include current drive [17,18], sheared poloidal flow drive [19], synergism with lower hybrid waves for enhanced current drive [14, 20], turbulence suppression [21] and channeling of power from fusion-born alpha particles [22]. Also, bulk ion heating is possible [23, 24].

In the JET experiments reported in this article, ICRF MC was investigated with ^{3}He in deuterium (D) or ^{4}He plasmas. The waves were tuned to a central fundamental ^{3}He resonance and the ^{3}He concentration was increased systematically from discharge to discharge using ^{3}He puffs. Figure 1 shows schematically the radial locations of the ion cyclotron resonance layers, the $n_{||}^2 = S$ ion-ion hybrid resonance layer and the $n_{||}^2 = S$ left-hand cutoff layer as a function of the ^{3}He concentration for representative parameters of these experiments. Here, $n_{||} = k_{||}c/\omega$ is the wave refractive index, and S and L are defined by Stix [26]. In this paper we will refer to the $n_{||}^2 = S$ ion-ion hybrid resonance layer as the ICRF MC layer. When the ^{3}He concentration was increased, the distance between the ICRF MC layer and the fundamental ^{3}He ion cyclotron resonance layer $\omega \approx \omega_c(^3\mathrm{He})$ was increased and a transition from ^{3}He minority heating to ICRF MC was observed, as expected.

In the ^{3}He minority heating regime, the launched fast waves are mainly absorbed by ^{3}He minority ions at $\omega \approx \omega_c(^3\mathrm{He})$, which results in the formation of a high-energy population, so called tail, in the resonating ^{3}He ion distribution function. The heating of the background plasma ions and electrons take place via collisions with the fast ^{3}He ions. When the energy of the fast ^{3}He ions is below the critical energy $E_{crit} \approx$ [25], the heating goes predominantly to ions. In the experiments discussed in this article, fast ^{3}He ions were measured with gamma ray emission spectroscopy.

The transition from ^{3}He minority heating to ICRF MC is due to changes in the wave polarisation with increasing ^{3}He concentration. As the ^{3}He concentration increases, the wave electric field component E_+, which rotates in the same direction as the ions and is important for ^{3}He minority damping, is reduced at the ^{3}He ion cyclotron resonance. Consequently, the single-pass ^{3}He damping decreases and the launched fast waves are mode-converted near the ICRF MC layer to short-wavelength waves. The maximum single-pass MC damping that can be achieved using fast waves

launched from a low-field side antenna is 25% [27]. A higher single-pass mode conversion damping of 100% is possible with fast waves propagating from the high-field side to the low-field side of the tokamak. This includes the fast waves that are launched on the low-field side of the tokamak, tunnel through the resonance-cutoff pair and are reflected back from the high-field side of the vessel. When the ^{3}He concentration increases further, both the single-pass ^{3}He ion cyclotron damping and the single-pass MC damping decrease. The ratio between the two mechanisms depends not only on the ^{3}He concentration, ion temperature and the wave spectrum but also on the possibility to form a high-energy tail of ^{3}He ions.

The nature of the short-wavelength waves depends on the scenario; they can be kinetic Alfvén waves, ion Bernstein waves and electromagnetic ion cyclotron waves, see for example [26, 28, 29]. Typically, these waves damp strongly by ELD because of an upshift of their poloidal mode numbers during the toroidal propagation of the waves, which leads to an upshift of $k_{||}$ [30]. This gives rise to direct electron heating on the short time scale of electron-electron collisions. As will be discussed in Section 2, we use ICRF power modulation to measure this direct electron power deposition [31, 3]. Our results presented in Section 3 demonstrate that efficient direct electron heating with ICRF MC is obtained on JET, with its spatial location controlled with the choice of the magnetic field, wave frequency and ion species mixture, in agreement with theory. In Section 4 experimental results are presented indicating the presence of competing ion heating mechanisms at high ^{3}He concentrations $n(^3He)/n_e$ of about 25% or larger. This is accompanied by a discussion on the ways to minimise such ion heating, if required. Finally, the results are summarised in Section 5.

2. OVERVIEW OF THE EXPERIMENTS

The experiments were carried out both in D and ^{4}He plasmas in the single-null divertor configuration at a magnetic field in the range of 3.4-3.7T and a plasma current in the range of 1.3-2MA. Up to 6MW of ICRF power was applied at frequencies of 33 or 37MHz using the four JET A2 ICRF antennas [32]. The fundamental ^{3}He ion cyclotron resonance was located centrally while the fundamental D and ^{4}He ion cyclotron resonance was off-axis on the high field side (Fig.2). The spread in the frequencies of the four antennas resulted in a typical spread of ≈10-15 and ≈5-10cm in the ICRF resonance layers for 33 and 37MHz, respectively. Dipole ($0\pi0\pi$) phasing of the antennas was used to launch waves with a symmetric toroidal mode number spectrum having $|N| \approx 26$ at the maximum of the antenna power spectrum and a full width at half maximum (FWHM) of $|\Delta N| \approx 14$ (N is the toroidal mode number). Asymmetric toroidal wave number spectra with $|N| \approx 16$ at the maximum of the antenna power spectrum and a FWHM of $|\Delta N| \approx 14$ were obtained with $+90^o$ (predominantly co-current launch) and -90^o (predominantly counter-current launch) phasing.

The ICRF power was square-wave modulated with a frequency of 10-20Hz and an amplitude of 50% to measure the direct electron power deposition using Fourier analysis [31] and break-in-slope analysis [3] of fast spatially-resolved electron temperature data. The electron temperature T_e was measured with electron cyclotron emission (ECE) heterodyne radiometer with a time resolution

of up to 0.5 ms and spatial uncertainty of ±3cm along a line-of-sight located about 13cm above the midplane of the vessel (cf. Fig.2). The T_e profile measured with the heterodyne radiometer was calibrated against the T_e profile measured with an absolutely-calibrated ECE Michelson interferometer, with a time resolution of 17ms and a line of sight about 35cm above the midplane of the vessel (cf. Fig.2). The total fraction of the ICRF power damped directly on electrons was estimated by integrating the measured electron power deposition over the plasma volume. Electron transport simulations [4] indicate that the effect of electron transport on the measured power deposition profiles is not negligible in the present experimental conditions. Indeed, the measured power deposition profiles are somewhat broader than those that need to be assumed in transport simulations in order to fit the amplitude and the phase of the T_e response to the ICRF modulation.

As was discussed in Section 1, the ^{3}He concentration plays a crucial role in determining the wave damping. The required ^{3}He concentration was obtained by puffing ^{3}He before and during the ICRF heating phase (cf. Fig.3). The He concentration $n(He)/n_e$ was estimated from the effective charge of ions and the relative concentration of deuterium and He deduced from the D_α and HeI light in the divertor and assuming that the plasma consists of He, deuterium and carbon impurity. In D plasmas with ^{3}He puffs the He concentration thus obtained was broadly consistent with the ^{3}He concentration inferred from the measured off-axis electron power deposition, assuming that the maximum power electron deposition takes place at the ICRF MC layer (Fig.4). In ^{4}He plasmas, roughly a factor of two larger ^{3}He puffs were typically required to obtain similar direct electron power deposition as in D plasmas, which is consistent with better confinement in D than in ^{4}He plasmas [33]. Information on the presence of fast ICRF-accelerated ions was obtained with gamma-ray spectroscopy [34] and high-energy neutral particle analysis [35].

3. DEMONSTRATION OF A TRANSITION FROM ICRH MINORITY HEATING TO MC HEATING WITH INCREASING ^{3}HE CONCENTRATION

To establish the conditions of ICRF MC with maximal direct electron heating, a series of discharges at 3.45T/1.8MA was carried out where the ^{3}He puff, applied before the ICRF power switch-on, was increased systematically from discharge to discharge. Figure 3a shows the key parameters for a discharge in this series. The waves were launched using -90^o phasing and a nominal frequency of 33MHz, placing the ^{3}He ion cyclotron resonance at $R\text{-}R_0 \approx$ 14-24cm. Low-power deuterium neutral beam injection was applied for diagnostic purposes.

As the ^{3}He puff, $\Gamma(^3\text{He})$, was increased, the T_e response to the ICRF power modulation changed gradually, indicating changes in the ICRF power deposition. In Fig.5, the T_e evolution during ICRF power modulation for a flux surface intersecting the ICRF MC layer is displayed for two discharges. The ^{3}He concentration $n(^3\text{He})/n_e$ as deduced from visible spectroscopy in the time-window of interest is about 4 and 21%, corresponding to a centrally located ICRF MC layer at $R \approx$ 3.1m and 2.8m, respectively (cf. Fig 1). The observed delay in the T_e response to the power modulation with $n(^3\text{He})/n_e \approx 4$ % is consistent with a larger contribution from indirect electron heating by ^{3}He minority ions.

With $n(^3He)/n_e \approx 21$ % the T_e response is prompter, consistent with stronger direct electron heating.

The average measured direct electron power density in the central plasma region within R = 2.7-3.3m along the line of sight of the ECE heterodyne radiometer for this series of discharges is shown in Fig.6 from break-in-slope analysis of the T_e data as a function of the ^{3}He concentration. For the ^{3}He concentrations in the range of 7 to 24 %, the ICRF MC layer is located centrally between ≈3.0 and ≈2.7 m. As we can see in Fig.6, the measured direct electron power density has a maximum at ^{3}He concentrations in the range of 12-20%, which we consider to be the range of optimal ^{3}He concentrations for direct electron damping with ICRF MC in the present plasma conditions. Both at higher and lower ^{3}He concentrations the direct electron power density decreases, suggesting the presence of competing power absorption mechanisms. At low ^{3}He concentrations, the main competing absorption mechanism is ^{3}He minority heating, which we discuss in detail later in this Section. The competing absorption mechanisms at high ^{3}He concentrations will be the topic of Section 4.

To investigate in more detail the changes in the direct electron power deposition profile with the ^{3}He concentration, a series of 3.45T/1.8MA discharges with different ^{3}He puffs was carried out with the ^{3}He cyclotron resonance located off-axis at $R-R_0 \approx -15$cm using a frequency of 37MHz. In this configuration, direct electron power deposition due to ICRF MC is off-axis on the high-field side of the ^{3}He cyclotron resonance, and thus could be distinguished from centrally located direct electron deposition due to fast wave TTMP and ELD. Furthermore, direct electron power deposition due to ICRF MC is expected to move further to the high-field side as the ^{3}He concentration is increased. Figure 7 shows the direct electron deposition profiles from break-in-slope analysis. As we can see in Fig. 7a, there is a transition from central to off-axis, more-peaked direct electron power deposition as the ^{3}He puff is increased. The results are consistent with the increase in the mode-converted power fraction and the movement of the ICRF MC layer to the high field side further away from the ^{3}He resonance, as the ^{3}He puff was increased. Integration of the measured direct electron power deposition profiles in Fig. 7a over the plasma volume shows that the direct electron power deposition increased from about 15 to about 70 % of the launched ICRF power as ^{3}He puff was increased from 0.8×10^{21} el in discharge 54244 to 2.4×10^{21} el in discharge 54249. These values are lower estimates for the actual direct electron damping due to the limited spatial coverage of the electron temperature measurement and difficulties to measure low power densities in the outer part of the plasma. The results are reproducible, as demonstrated by the power deposition profiles shown in Fig.7b for discharges prepared in the same way. An estimate for the ^{3}He concentration in the ^{4}He discharges with ICRF only heating in Fig.7 was obtained by assuming that the maximum off-axis direct electron power deposition coincides with the ion-ion hybrid resonance layer. This gives $n(^3He)/n_e \approx 10$ % for discharges 54249 and 54250 with highest ^{3}He puffs, which is below the optimum ^{3}He concentration for ICRF MC deduced from Fig. 6.

In the plasmas reported in this paper, the phase velocity of the waves around the maximum of the antenna power spectrum is close to the electron thermal velocity in the ICRF MC layer, which gives rise to strong electron damping in the immediate vicinity of the layer. In such conditions, the

broadening of the power deposition profile is mainly due to the vertical extent of the ICRF MC layer, while the spread in the ICRF frequencies plays a smaller role for the direct electron power deposition width. Simulations with the full-wave ALCYON code coupled with the ray-tracing RAYS code [36] for discharge 54256, taking into account the full antenna spectrum, show somewhat more peaked direct electron power deposition profiles (Fig.8) than those measured (Fig.9). The difference is attributed to the effect of electron heat transport on the measured deposition profiles discussed in Section 2. According to the ALCYON+RAYS simulations, the damping of the mode-converted short-wavelength waves occurs near the ICRF MC layer. Thus, the location of the power deposition is not significantly modified by the propagation of the short-wavelength waves in the present experimental conditions. The measured power deposition has a typical full width at half maximum (FWHM) of about 30cm for a peak deposition inside $r/a < 0.7$. In comparison, the direct electron power deposition profiles with dominant fast wave TTMP+ELD are central and significantly broader, with a typical FWHM of 50-60cm in these plasma conditions (c.f. profile for discharge 54249 at t = 12.03 s in Fig. 12). The -90^{o}, $+90^{o}$ and dipole ($0\pi0\pi$) phasings give rise to similar direct electron power deposition profiles in the ICRF MC regime, with somewhat more peaked and larger direct electron power density profiles with -90^{o} phasing (Fig. 10). This difference is attributed to stronger competing absorption mechanisms with $+90^{o}$ and dipole phasings, as will be discussed in detail in Section 4.

Changes in the measured direct electron deposition locations were accompanied by changes in the electron temperature profiles. With ICRF MC with a frequency of 33 MHz at a magnetic field of 3.7T, a higher power density and more peaked electron temperature profile were obtained than with more off-axis MC at a magnetic field of 3.45T, as illustrated in Fig.11.

The power deposition profiles and electron temperature profiles shown in Figs 7, 10 and 11 are those at the beginning of an ICRH flat-top in discharges with ^{3}He puff applied before ICRH. During an ICRH flat-top with a typical duration of 4–6 s (i.e. ≈15-40 energy confinement times) in these discharges, the ^{3}He concentration decreased slowly in time (cf. Fig. 3), which lead to a time-evolving direct electron power deposition. In particular, the location of the maximum direct electron heating moved in time and the total power deposited directly on electrons decreased (Fig.12). The observed evolution is consistent with the simulated power partitioning between ^{3}He minority heating and ICRF MC as given by the PION code [37, 38], showing an increase in the ^{3}He minority damping and a decrease in electron damping as the ^{3}He concentration is decreased. Experimentally, the increase in ^{3}He minority heating in time in a given discharge was suggested by an increase in the bulk ion temperature and in the D-D fusion reactivity of the thermal plasma towards the end of the ICRF phase in plasmas with ICRF heating only (Fig.13). The increase in the bulk ion temperature and the D-D fusion reactivity is consistent with an increasing population of low-energy ^{3}He minority ions which heat predominantly the bulk ions.

Experimental evidence for the suppression of the high-energy ^{3}He ion population as the ^{3}He puff was increased from discharge to discharge was given by gamma-ray emission spectroscopy

[34]. The gamma-ray energy spectra integrated over the ICRF heating phase are shown in Fig. 14 for a number of discharges with different ^{3}He concentrations. The peaks in the spectra are due to nuclear reactions between fast ^{3}He ions and ^{9}Be and ^{12}C impurity ions, which can take place when the energy of the fast ^{3}He ion reaches the range of 1MeV. These peaks and therefore the number of fast ^{3}He ions become smaller and finally disappear as the ^{3}He concentration increases, as expected.

Further confirmation for the changes in the plasma heating characteristics as the ^{3}He puff was increased comes from the sawtooth activity. Sawteeth are plasma internal relaxations that occur when the on-axis safety factor q drops below 1 and are sensitive to the electron temperature and plasma current profile. Furthermore, they can be stabilised by fast ions inside the q = 1 surface [39]. Figure 15 shows the sawtooth activity for a number of discharges with different ^{3}He puffs applied before the ICRF phase. In all discharges, there are no sawteeth before the application of ICRH as the q on axis is above one. As the plasma is heated, the plasma current profile evolves and the on-axis q drops, resulting in the appearance of sawteeth. At low ^{3}He puffs sawtooth stabilisation occurred as soon as the sawteeth appeared due to the stabilising effect of fast ^{3}He ions heated at the centrally located resonance at $R-R_0 \approx 14$ cm. As the ^{3}He puff was increased, the sawtooth stabilisation occurred later. These differences appear to be consistent with a transition from the ICRF MC regime to the ^{3}He minority regime as the ^{3}He concentration in the discharge decays in time, resulting in an increase in the fast ion pressure inside the q=1 surface and subsequently in sawtooth stabilisation.

In order to sustain efficient ICRF MC throughout the ICRF phase (i.e. to avoid the decrease in the ^{3}He concentration which resulted in an increase in competing ^{3}He minority damping), ^{3}He puff during the ICRF phase was found necessary. With a correctly programmed ^{3}He flow, it was possible to keep the direct electron power deposition constant in time (Fig.9). With central ICRF MC, this resulted in quasi-steady-state discharges with peaked electron temperature profiles and $T_e(0)$ in excess of 8 keV for $n_e(0) \approx 3\times10^{19}m^{-3}$ for 5MW of ICRF power alone (cf. Fig.16). The energy confinement time, $\tau_E \approx 0.28$s, corresponds to an ELMy H mode quality factor, ITERH97-P [40], of 0.7, indicating good-quality L-mode confinement. So far, ICRF MC has been used successfully on JET in combination of up to 15MW of NBI power and 3MW of LHCD power both in L-mode and H-mode discharges. In the experiments reported in this paper, the ^{3}He flow required to keep the power deposition constant in time was adjusted based on the measured decay of the ^{3}He concentration in previous similar discharges. Real time control of the ^{3}He concentration has now been developed to improve further the practical applicability of ICRF MC on JET.

4. COMPETING DAMPING MECHANISMS ABOVE THE OPTIMAL ^{3}HE CONCENTRATION FOR ICRF MC

As was discussed in Section 3, the measured direct electron power deposition profiles suggest an optimal ^{3}He concentration in the range of 12-20% for maximal electron damping with ICRF MC (cf. Fig.6). At lower ^{3}He concentrations, the main competing absorption mechanism is ^{3}He minority heating discussed in detail in Sections 1 and 3. In this section we will concentrate on the competing

absorption mechanisms at ^{3}He concentrations above the optimal one for direct electron heating with ICRF MC.

We start by investigating three 3.7T/ 2MA discharges shown in Fig.17 with identical ^{3}He puff and ICRF power applied at 33MHz, but with different phasings. In all discharges, low power deuterium beam injection was applied and the ^{3}He concentration was similar, decreasing from about 35% at the beginning of the ICRF phase to about 25% at the end of the ICRF phase. The direct electron power deposition was central as shown in Fig.11 for discharge 53818 at t = 7 s. As we can see in Fig. 17, the neutron rate with dipole phasing is larger by almost a factor of two than with +90^o phasing, while the neutron rate with +90^o phasing is a factor of two larger than with –90^o phasing. There is also a small difference in the plasma diamagnetic energies and the electron temperatures. The ion temperatures measured at r/a ≈ 0.3 with an x-ray crystal spectrometer are similar ($T_i \approx 2.4$keV) indicating that the differences in the fusion reactivity cannot be due to differences in the bulk ion temperatures. In fact, these differences are due to different fast deuteron populations with energies above the maximum beam injection energy of 135keV. The presence of such deuterons is confirmed by the measured gamma-ray emission spectra, which show clear gamma lines from nuclear reactions between fast deuterons and carbon impurity (Fig. 18a). The reactions between carbon and fast deuterons can take place when the energy of the deuteron is about 0.9MeV or larger [34]. Independent measurements with another device, a high-energy neutral-particle analyser [35], show that the deuteron distribution functions extend into the MeV range. The gamma-ray emissivity (Figs 18a and b), neutron rate and fast deuteron atom fluxes are significantly reduced when the magnetic field is reduced from 3.7 to 3.45T (keeping the safety factor q fixed).

The presence of fast deuterons with energies above the maximum beam injection energy indicates that some wave power is absorbed by the fast beam-injected deuterons. Since interaction between ions and short-wavelength waves, such as ion Bernstein waves, is not capable of creating fast ion populations [28], a more likely explanation for our observations is interaction of beam deuterons with a wave with a longer wavelength, such as the fast wave. A high-amplitude driven contained mode has been suggested [41] to explain similar fast ion observations with ICRF MC on TFTR[42, 43, 22].

The observed differences in the fast deuteron populations with different antenna phasings suggest that the waves interacting with the fast deuterons have different directivities for different antenna phasings. The wave directivity plays an important role in the resonance condition for NBI-injected deuterons via the Doppler broadening which depends on the parallel wave vector $k_{||}$ and the deuteron parallel velocity $v_{||}$. Numerical calculations solving the wave equations in the ICRF MC region [44] indicate strong wave fields in the vicinity of the ICRF MC layer. If the resonance condition is fulfilled for a NBI-injected deuteron in the vicinity of the ICRF MC layer due to the large Doppler shift, strong wave-particle interaction can occur in spite of the high D concentration [45].

Figure 19 shows the radial location of the ICRF MC layer, ^{3}He and D ion cyclotron resonance layers and Doppler-broadened ion cyclotron resonance layer for 135 keV beam deuterons injected in the co-current direction as a function of the toroidal wave number N for a number of $n(^3He)/n_e$.

Here, the parameters of the discharges shown in Fig.17 are used and the parallel wave vector equal to $k_{||} = N/R$ is assumed. As N increases, the distance between the Doppler-broadened cyclotron resonance of beam deuterons and the ICRF MC layer decreases until the layers overlap. For $n(^3He)/n_e \approx 30$ %, this occurs for N in the range of 30. Such mode numbers are typical in the antenna power spectrum for dipole phasing and also contribute to the spectrum for $\pm 90^o$ phasings (cf. Section 2 and Fig.14b in Ref. 32), with a larger contribution for $+90^o$ than for -90^o phasing. In reality, the parallel wave vector $k_{||} = NB_\varphi/(RB) + mBq/(rB)$ depends not only on the toroidal mode number N, as is assumed in Fig.19, but also on the poloidal mode number m. The correction due to the poloidal mode number, which is not a quantum number, can be important as it can further broaden the cyclotron resonance of the deuterium beam ions. From Fig.19 we expect the strongest interaction with waves propagating in the co-current direction with largest N, in agreement with the experiments reported in this paper. We also recall that the measured fast deuterium populations were weaker when the magnetic field was decreased from 3.7 to 3.45T (cf. discussion on Fig.18), which moved the layers shown in Fig. 19 by about 20cm to the high-field side. The weaker deuterium populations at 3.45T can be understood to be due to a lower power density and thus weaker wave-particle interaction with a more off-axis resonance. At lower ^3He concentrations the ICRF MC layer is further away from the unshifted deuterium cyclotron resonance layer, and larger toroidal mode numbers of the fast wave or higher energy beam-injected deuterons are required to Doppler-broaden the beam cyclotron resonance to the ICRF MC region.

The above results suggest that using waves propagating in the counter-current current direction minimises the competing ion damping in the presence of deuterium beams injected in the co-current direction. An experimental estimate for the difference in total ion absorption between waves launched predominantly in the co-current and counter-current direction ($+90^o$ and -90^o phasing, respectively) was obtained from discharges shown in Figs 20 and 21. By integrating over the plasma volume the measured direct electron power deposition profiles shown in Fig. 20b and by attributing the remaining power as being absorbed by ions, we estimate that $+90^o$ phasing gives about 35 % larger ion damping than -90^o phasing. A similar estimate is obtained from the analysis of discharges shown in Fig. 21, with the same neutron yield but lower ICRF power with $+90^o$ phasing.

The acceleration of deuterium beam ions with dipole phasing in the ICRF MC regime was investigated in more detail using two different ICRF heating schemes in deuterium plasmas at 3.45T/2MA (Fig. 22a). In discharge 55712 ^3He puff was applied to obtain ICRF MC with $n(He)/n_e \approx 20$-25% using an ICRF frequency of 33MHz. In discharge 55714, the ^3He puff used in discharge 55712 was replaced by a similar ^4He puff so that ^3He minority heating of the residual ^3He minority ions remaining in the vessel from the previous discharges was obtained in as identical plasma conditions as possible to those of discharge 55712. The ICRF frequency used in discharge 55714 was 37MHz, so that the location of the power deposition was as close as possible to the one in discharge 55712 (Fig.22b). Short-duration deuterium beam pulses were applied in both discharges, and the resulting build-up and decay of the fast deuteron population were monitored from the fusion reactivity.

With predominant ^{3}He minority heating in discharge 55714, the decay of the neutron rate takes place in about 200 ms following the switch off of the deuterium NBI, which is consistent with the classical slowing down time of about 200 ms for the deuterium beam ions from their maximum injection energy of 122 keV. With ICRF MC in discharge 55712, the rate of rise of the neutron rate is faster and the total neutron rate is higher during the beam injection, indicating acceleration of deuterium beam ions. After the beam switch-off in discharge 55712, it takes a longer time, i.e. about 2 s, for the neutron rate to decrease to the same level as before the beam pulse. This decay time corresponds to a slowing down time of deuterons with energy in the MeV range in the present conditions. At the end of the beam pulse the neutron profile is significantly broader in discharge 55712 (Fig. 23), suggesting that the deuterium absorption takes place off-axis, which is consistent with the off-axis location of D beam ion damping.

CONCLUSIONS

Efficient on-axis and off-axis direct electron heating have been obtained with ICRF mode conversion using $\omega \approx \omega_c(^3\text{He})$ in JET deuterium and ^{4}He plasmas. The parametric dependence of the location of the direct electron power deposition has been found to be consistent with theoretical expectations for ICRF MC. The optimal ^{3}He concentration to maximise the direct electron damping in these plasmas is found to be about 12-20%. At low ^{3}He concentrations ^{3}He minority heating is an important competing ion damping mechanism, as expected. At high ^{3}He concentrations in the presence of deuterium neutral beam injection in the co-current direction, damping on deuterium beam ions takes place. This damping is minimised with waves launched in the counter-current direction.

ACKNOWLEDGEMENTS

It is a pleasure to thank our colleagues at JET who operated the tokamak, the heating systems and the diagnostics during these experiments. The work was performed under the European Fusion Development Agreement. The work carried out by the UKAEA personnel was partly funded by the UK department of Trade and Industry.

REFERENCES

[1]. A. Becoulet, Plasma Phys. Control. Fusion **38** A1 (1996).
[2]. L.-G. Eriksson and T. Hellsten, Nucl. Fusion **29** 875 (1989).
[3]. D.F.H. Start, et al., Nucl. Fusion **30** 2170 (1990).
[4]. P. Mantica et al., 19th IAEA Fusion Energy Conference, 14–19 October 2002, Lyon, France, paper EX/P1-04.
[5]. Equipe TFR, IAEA-CN-41/I-2.
[6]. Y. Takase et al., Plasma Phys. Control. Fusion **38** 2215 (1996).
[7]. R. Majeski et al., Phys. Plasmas **3** 2006 (1996).
[8]. R. Majeski et al., Phys. Rev. Lett. **76** 764 (1996).

[9]. B. Saoutic, A. BÈcoulet, T. Hutter, and D. Fraboulet, Phys. Rev. Lett. **76**, 1647 (1996).
[10]. P.T. Bonoli et al., Phys. Plasmas **4** 1774 (1997).
[11]. S.J. Wukitch et al., IAEA-F1-CN-69/CDP/10 Yokohama 1998.
[12]. I. Monakhov et al., 26th EPS Conf. on Controlled Fusion and Plasma Physics, Maastricht, Europhysics Conference Abstracts, Vol. **23J** (1999) OR12.
[13]. J.-M. Noterdaeme et al., 26th EPS Conf. on Controlled Fusion and Plasma Physics, Maastricht, Europhysics Conference Abstracts, Vol. **23J** 1561 (1999).
[14]. C. Gormezano et al., in Radio Frequency Power in Plasmas, AIP Conference Proceedings No 289 (AIP, New York, 1993), p. 87.
[15]. X. Litaudon et al., 26th EPS Conf. on Controlled Fusion and Plasma Physics, Maastricht, Europhysics Conference Abstracts, Vol. **23J** 965 (1999).
[16]. D.J. Gambier et al., Nucl. Fusion **30** 23 (1990).
[17]. A.K. Ram and A. Bers, Phys Fluids **B3** 1059 (1991).
[18]. R. Majeski, C.K. Phillips and J.R. Wilson, Phys. Rev. Lett. **73** 2204(1994).
[19]. L.A. Berry, E.F. Jaeger, D.B. Batchelor, Phys. Rev. Lett. **82** 1871 (1999).
[20]. A.K. Ram et al., in Proc. 21st European Conference on Controlled Fusion and Plasma Physics, Montpellier, France, 1994 (European Physical Society, Geneva, 1994), Vol. **18B**, Pt III, p. 1134.
[21]. G.G. Craddock, P.H. Diamond, M. Ono and H. Biglari, Phys. Plasmas **1** 1944 (1994).
[22]. N.J. Fisch, Nucl. Fusion **40** 1095 (2000).
[23]. M. Porkolab, Phys. Rev. Lett. **54** 434 (1985).
[24]. F. Nguyen et al., 29th EPS Conf. on Controlled Fusion and Plasma Physics, Montreux, Europhysics Conference Abstracts, Vol. **26B** (2002) P-1.045.
[25]. T.H. Stix, Plasma Physics **14** 367 (1972).
[26]. T.H. Stix, Nucl. Fusion **15** 737 (1975).
[27]. K.G. Budden, *Radio Waves in the Ionosphere*, Cambridge University Press, Cambridge, 1961.
[28]. M. Ono, Phys. Fluids **5** 241 (1993).
[29]. F.W. Perkins, Nucl. Fusion **17** 1197 (1977).
[30]. A.K. Ram and A. Bers, Phys. Fluids **B3** (1991) 1059.
[31]. D.J. Gambier, et al., Nucl. Fusion **30** 23 (1990).
[32]. A. Kaye, et al., Fusion Engineering and Design **24** 1 (1994).
[33]. V.Phillips, Proc. 28th EPS Conference on Controlled Fusion and Plasma Physics, Funchal, 2001, Europhysics Conference Abstracts Vol. 25 A (European Physical Society, Geneva, 2001) P4.118.
[34]. Kiptily V.G. et al., Nucl. Fusion **42** 999 (2002).
[35]. Korotkov, A.A., Gondhalekar, A., and Stuart, A.J., Nucl. Fusion **33** 35 (1997).
[36]. Yu. Petrov, A. BÈcoulet., I. Monakhov, Phys. Plasmas 7 911 (2000).
[37]. L.-G. Eriksson and T. Hellsten, Phys. Scripta **55** 70 (1995).
[38]. L.-G. Eriksson, T. Hellsten, and U. Willén, Nucl. Fusion **33** 1037 (1993).

[39]. F. Porcelli, Plasma Phys. Control. Fusion **33** 1601 (1991).
[40]. ITER Confinement Database and Modelling Working Group (presented by J.G. Cordey), Plasma Phys. Control. Fusion **39** B115 (1997).
[41]. D.S. Clark and N.J. Fisch, Phys. Plasmas **7** 2923 (2000).
[42]. D.S. Darrow et al., Phys. Plasmas **3** 1875 (1996).
[43]. D.S. Darrow et al., Nucl. Fusion **36** 509 (1996).
[44]. M.J. Alava and J.A. Heikkinen, Phys. Scripta **45** 345 (1992).
[45]. T. Hellsten et al., in Radio Frequency Power in Plasmas (AIP Conference Proceeding 595), (AIP, New York, 2002), p. 377.

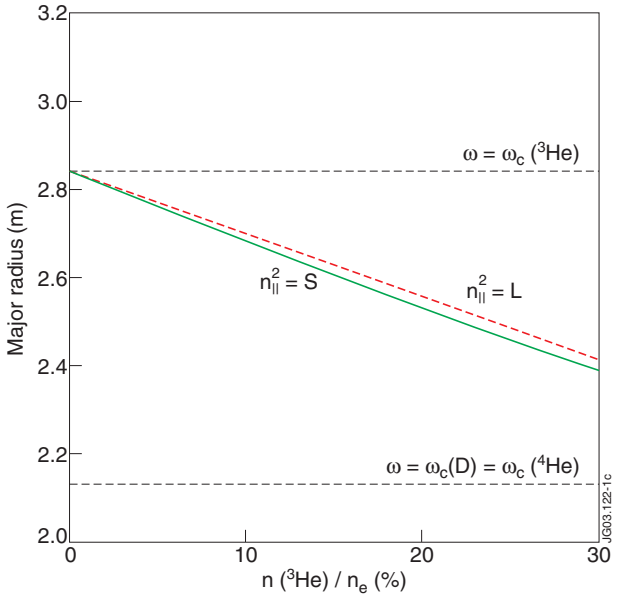

Figure 1: Radial locations of the ion cyclotron resonance layers and $\omega = \omega_c(^4He) = \omega_c(D)$, the $n_{||}^2 = S$ ion-ion hybrid resonance layer and the $n_{||}^2 = L$ left-hand cutoff layer as a function of the ^3He concentration assuming $B=B_0R_0/R$, B_0= 3.45T, R_0 = 3m, $n_e = 3\times10^{19}$ m^{-3}, $n_{||}^2 = 0$, a wave frequency of 37MHz and a plasma consisting of ^3He and D. When the wave frequency is decreased to 33MHz, the major radii of the layers increase by about 10%. When the magnetic field is increased from 3.45 to 3.7T, the major radii of the layers increase by about 7%.

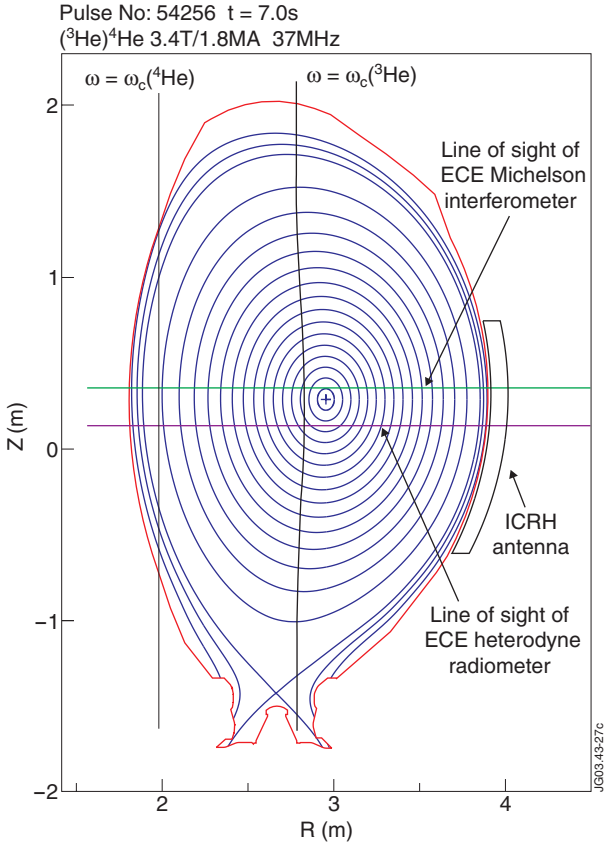

Figure 2: Locations of the ^3He and ^4He ion cyclotron resonance layers for discharge 54256 with B ≈3.45T and an ICRF frequency of 37MHz. Also, the ICRH antenna and the two lines-of-sight of electron temperature measurements are shown.

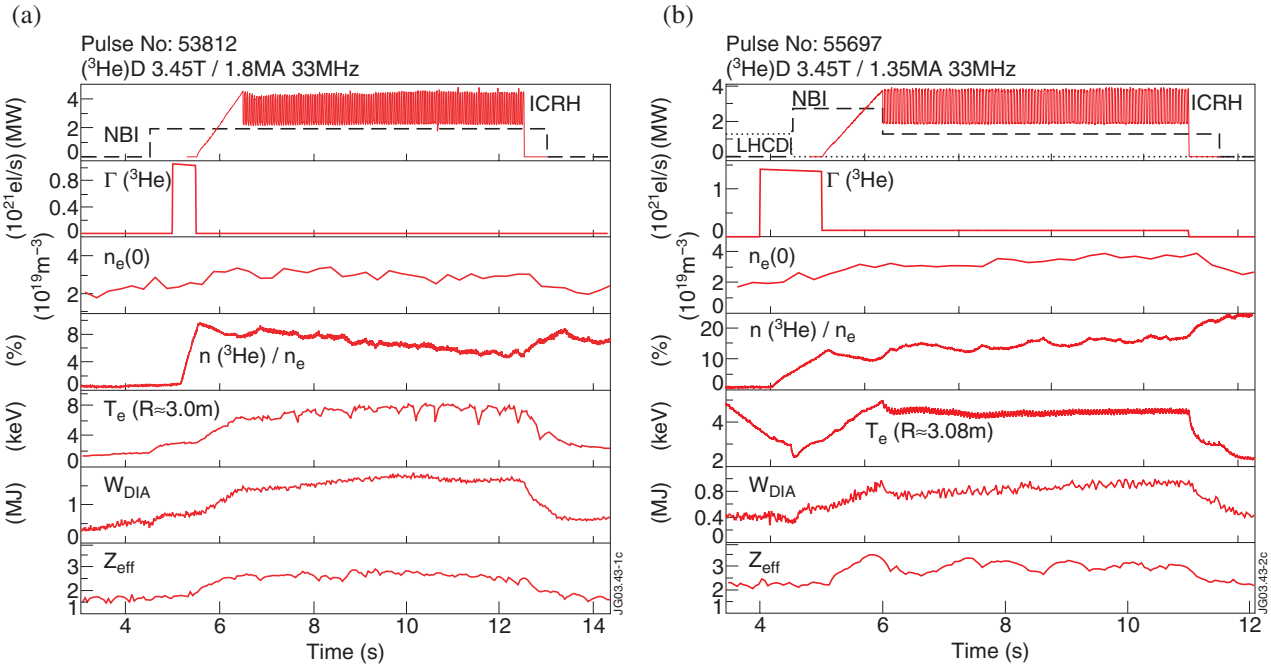

Figure 3: ICRF and NBI power, ^3He flow rate, central electron density, ^3He concentration, central electron temperature, plasma diamagnetic energy and effective charge of ions for two discharges with ICRF MC: (a) a discharge with ^3He puff only before the application of ICRH and (b) a discharge with ^3He puff before and during ICRH.

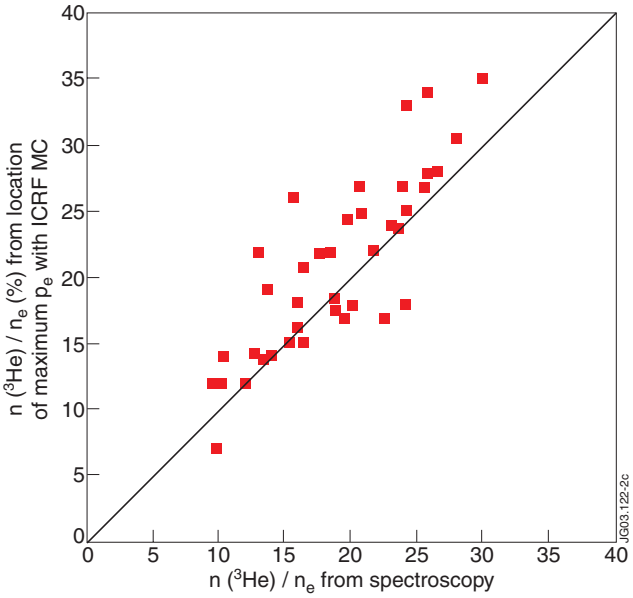

Figure 4: Correlation between the ^{3}He concentration deduced from spectroscopic data and the ^{3}He concentration deduced from the measured direct electron power deposition due to ICRF MC with ^{3}He in deuterium plasma.

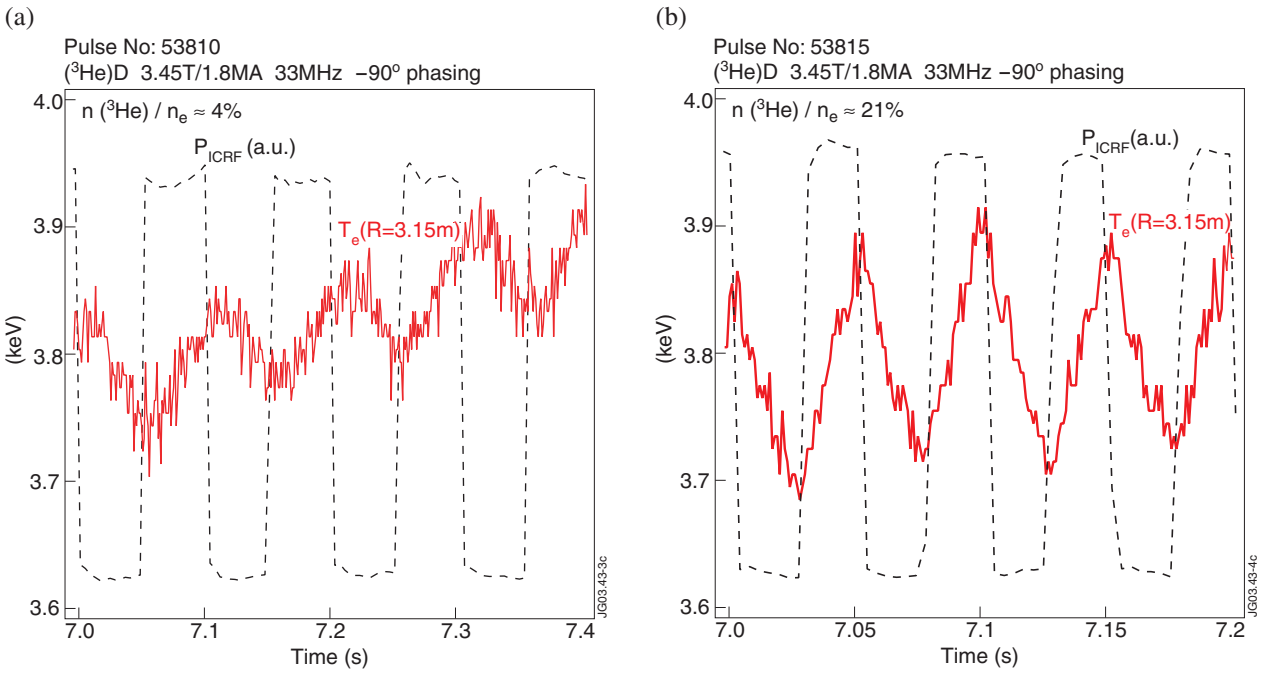

Figure 5: Electron temperature response to modulated ICRH on a flux surface intersecting the ICRF MC layer for discharges 53810 and 53815 with a ^{3}He concentration of ≈4 and 21%, respectively.

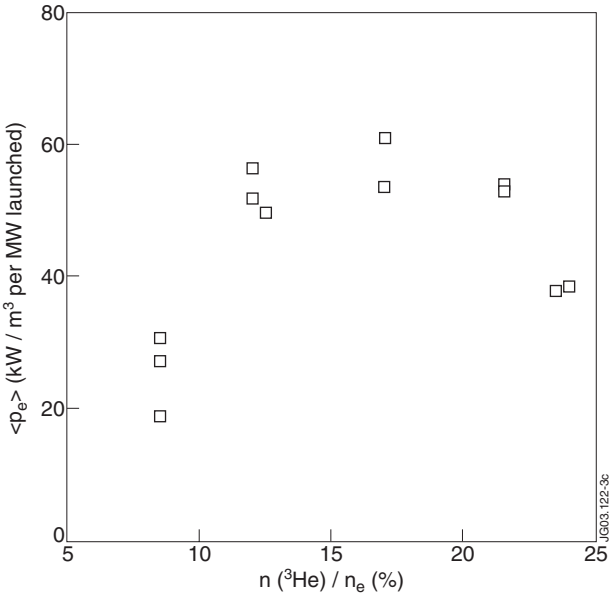

Figure 6: Average measured direct electron power density in the central plasma within R = 2.7-3.3m along the line of sight of the ECE heterodyne radiometer from break-in-slope analysis of T_e data (deuterium discharges 53812-53815 and 53817 with ICRH using 33MHz and -90^o phasing).

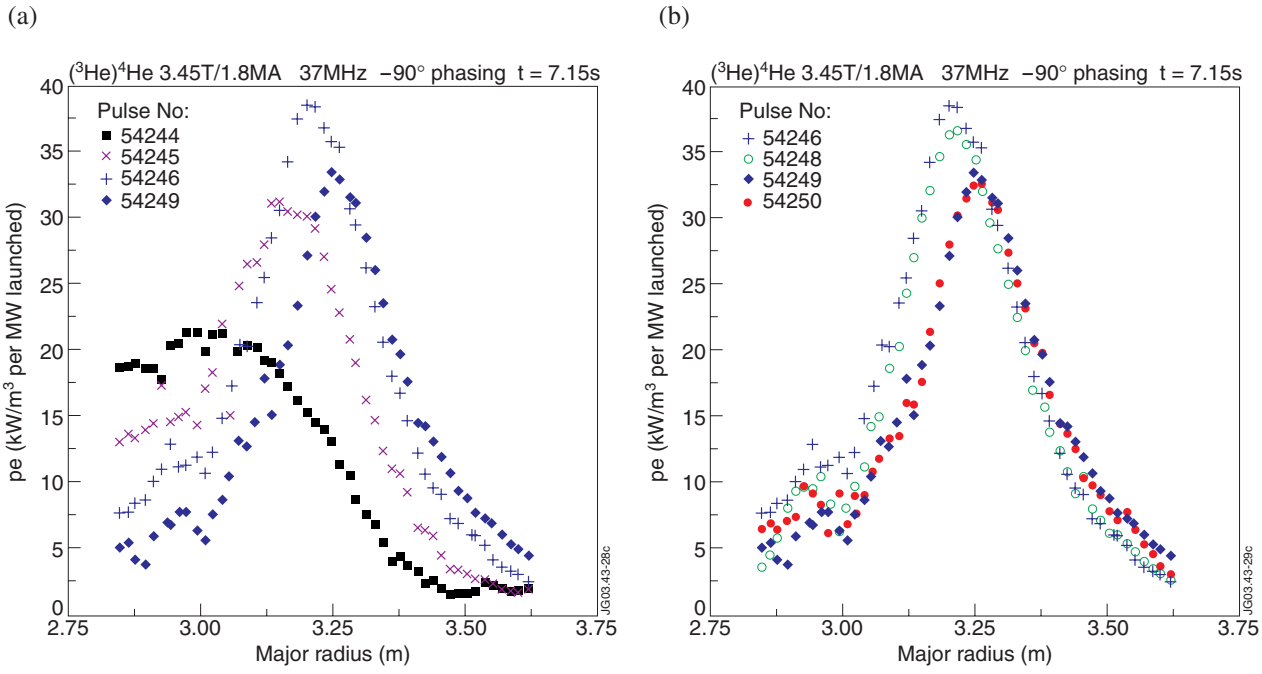

Figure 7: Direct electron heating profiles from break-in-slope analysis of T_e data (a) for four ^{4}He discharges prepared in the same way except for different ^{3}He puffs and (b) for two pairs of ^{4}He discharges prepared in the same way, including similar ^{3}He puffs. The ^{3}He puffs are 0.8×10^{21} el in discharge 54244, 1.3×10^{21} el in discharge 54245, 1.9×10^{21} el in discharges 54246 and 54248, 2.4¥10^{21} el in discharge 54249 and 2.3×10^{21} el in discharge 54250. The horizontal axis is the major radius along the T_e measurements.

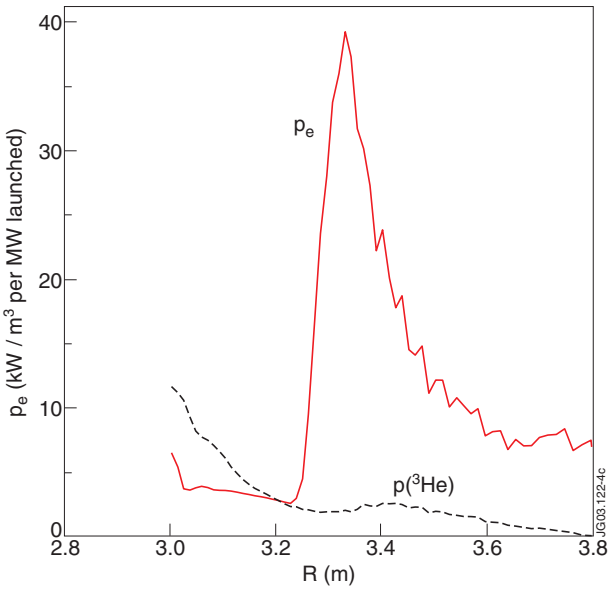

Figure 8: Calculated power deposition profiles as given by ALCYON+RAYS for discharge 54256, mirrored versus the magnetic axis to facilitate the comparison with experimental data shown in Fig. 9.

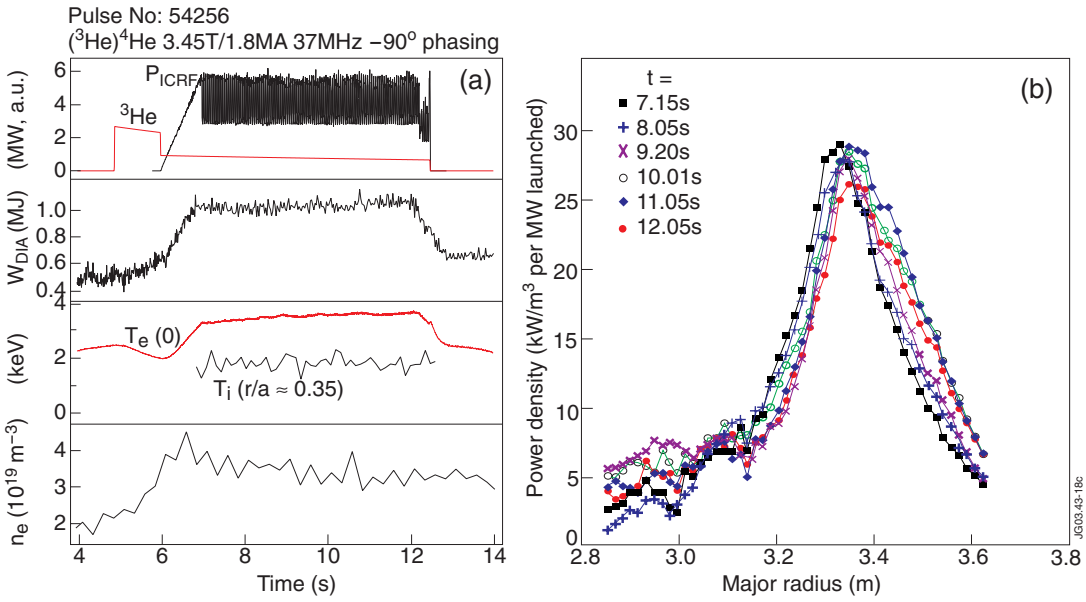

Figure 9:(a) Overview of the main plasma parameters and (b) direct electron power deposition profiles from break-in-slope analysis of T_e data for discharge 54256.

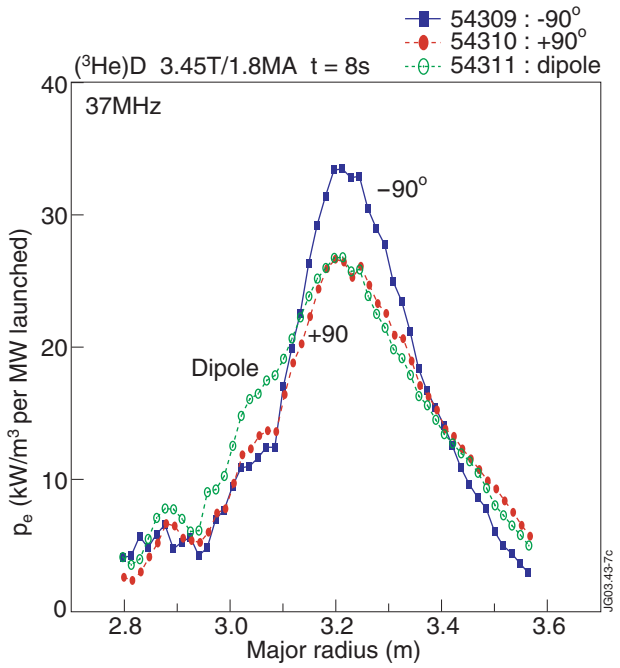

Figure 10: Direct electron power deposition profiles deduced from break-in-slope analysis of T_e data for +90°, -90° and dipole phasings.

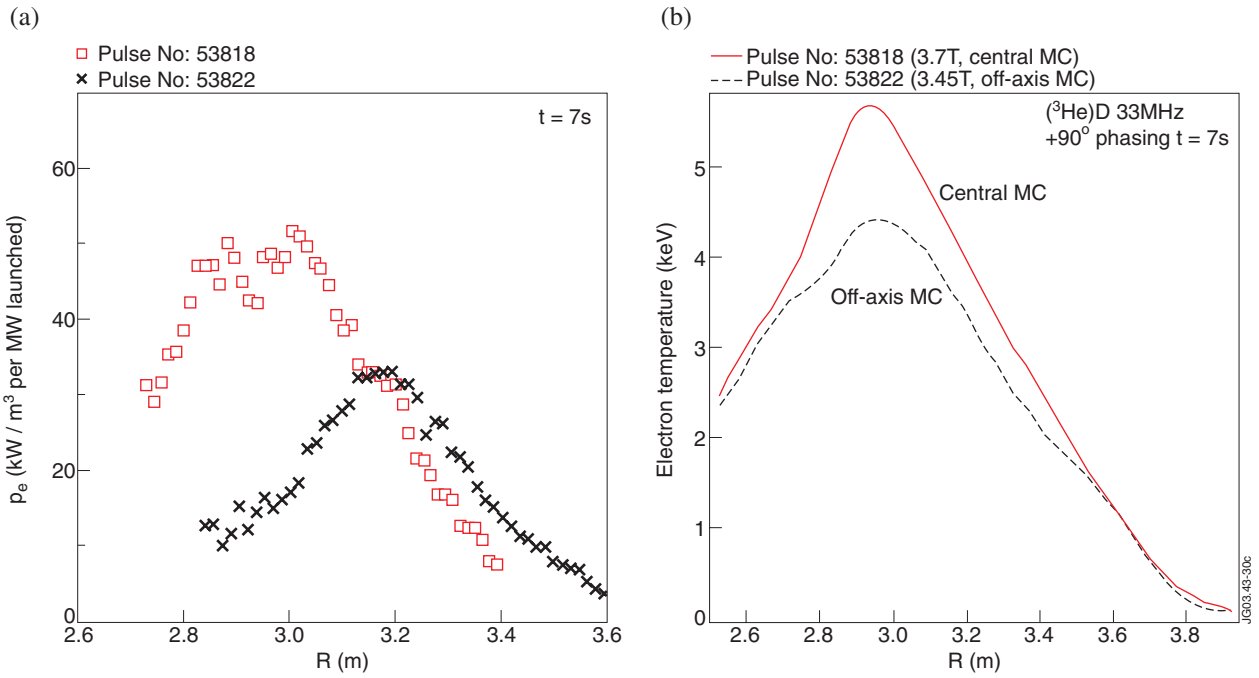

Figure 11: (a) Measured direct electron power deposition profile from break-in-slope analysis of T_e data and (b) electron temperature profile for two discharges with ICRF MC using a frequency of 33MHz at 3.45 and 3.7T, respectively. An average ICRF power of 3.45MW is used in combination with 2MW of diagnostic deuterium beam power.

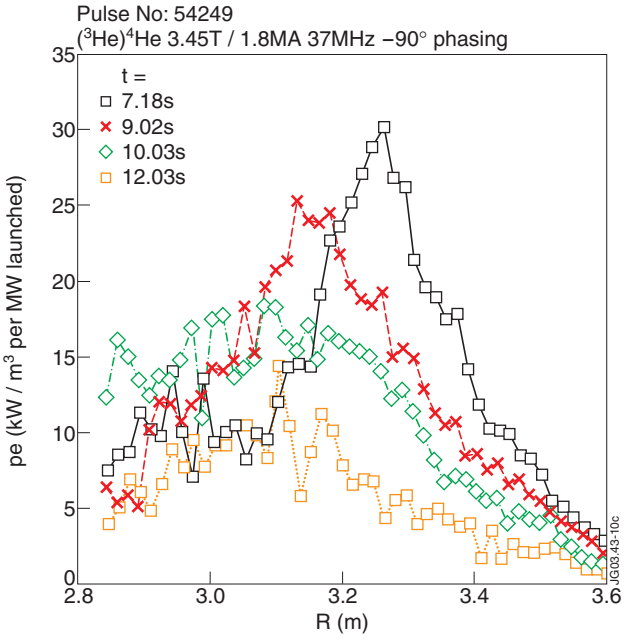

Figure 12: Time evolution of the direct electron power deposition profile from break-in-slope analysis of T_e data for discharge 54249. The ^{3}He puff was applied before switch-on of ICRH at t = 6s (cf. Fig. 13).

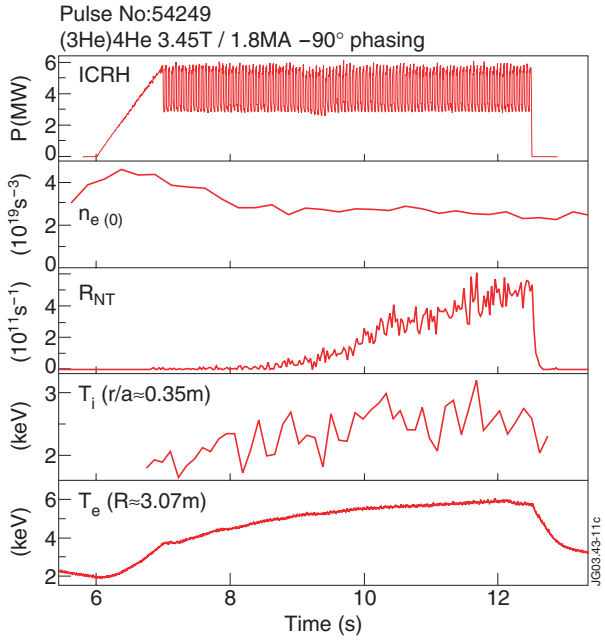

Figure 13: Overview of the main plasma parameters for discharge 54249 with ICRF heating alone using $\omega \approx \omega(^3He)$ in ^{4}He with $n_D/n_e \approx 3\%$.

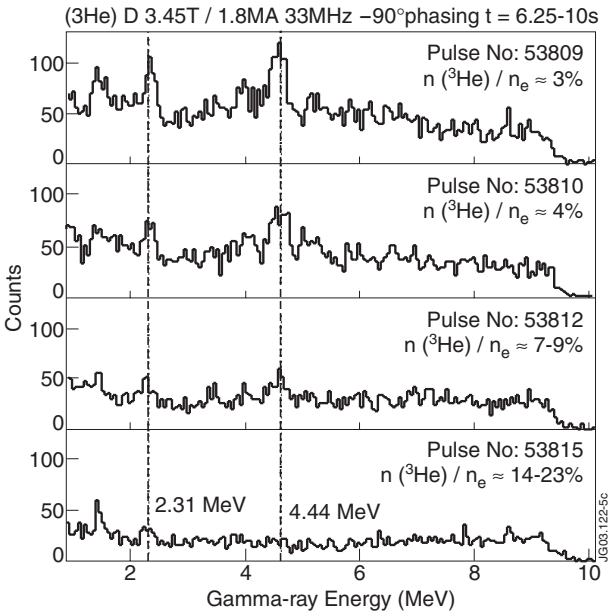

Figure 14: Gamma ray energy spectra for four discharges with different ^{3}He puffs applied before ICRH. Gamma lines are predominantly from reactions $^9Be(^3He,p\gamma)^{11}B$ and $^{12}C(^3He,p\gamma)^{14}N$ (gamma lines at 2.31 and 4.44MeV). The ^{3}He concentrations for each discharge are also shown.

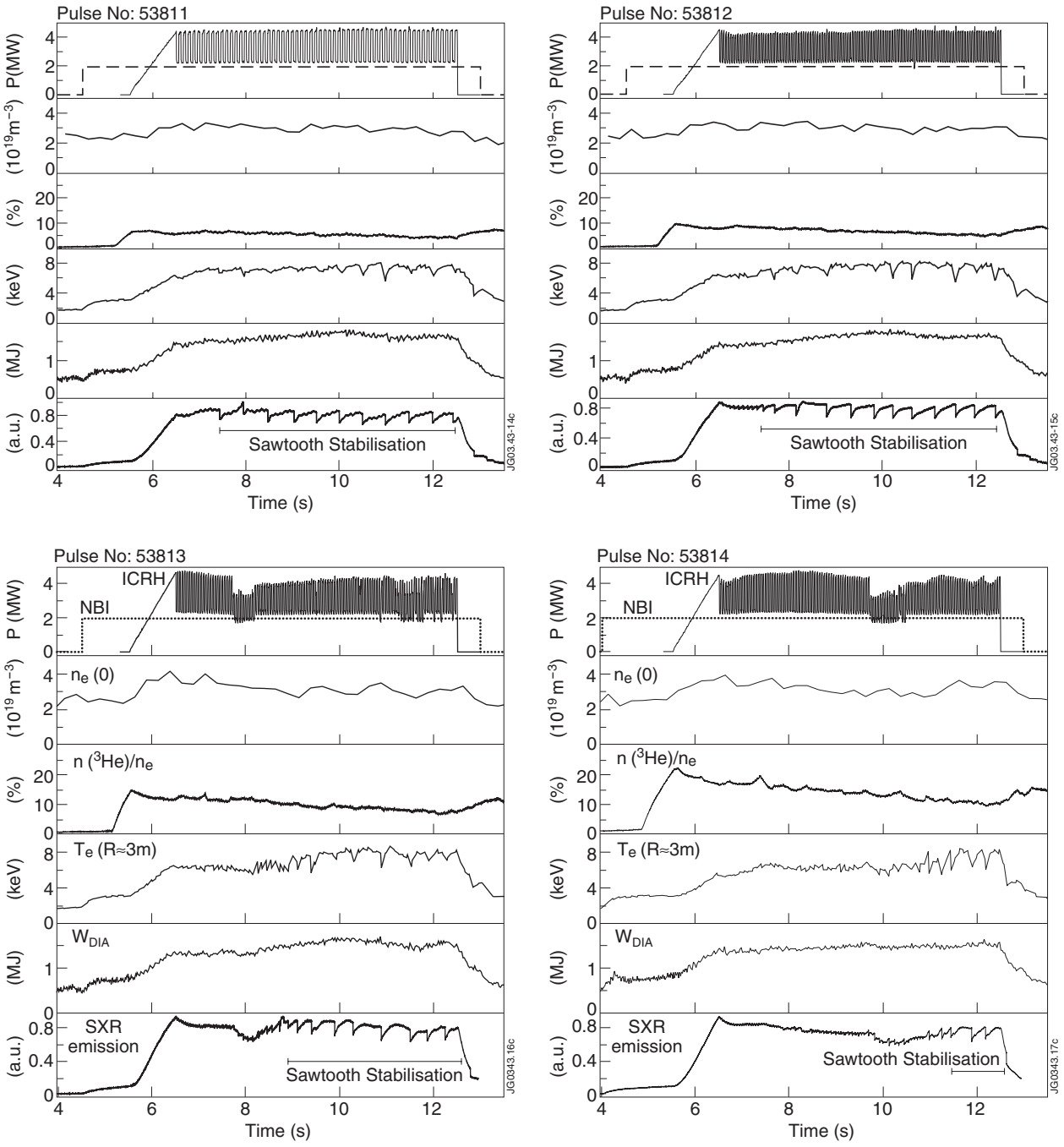

Figure 15: ICRH and NBI power, central electron density, ^{3}He concentration, electron temperature, plasma diamagnetic energy and soft x-ray emission for a number of 3.45T/1.8MA deuterium discharges with ICRF heating using a frequency of 33MHz.

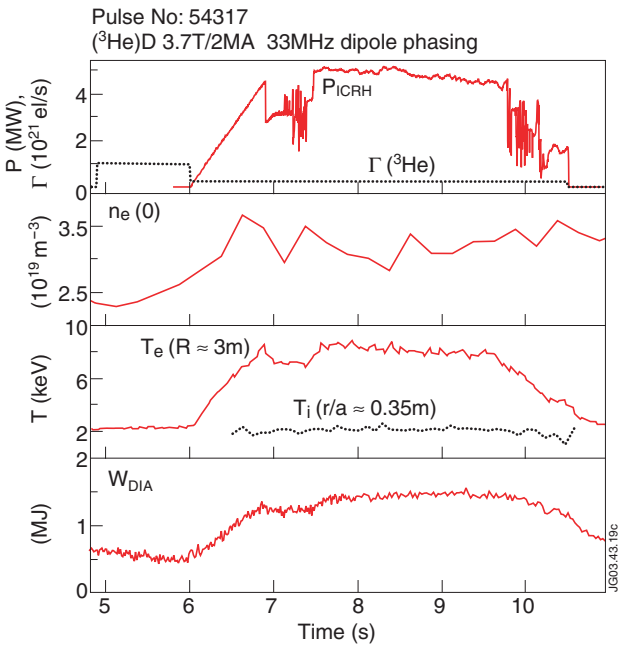

Figure 16: Overview of the main plasma parameters for discharge 54317 with a record T_e obtained with central ICRF MC heating only and ^{3}He puff throughout the ICRH phase.

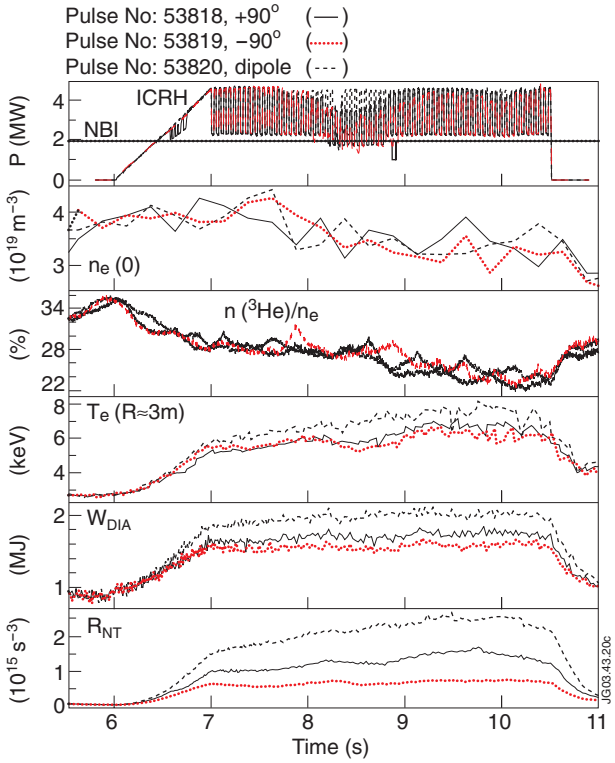

Figure 17: Overview of three discharges with +90°, −90° and dipole phasing with central ICRF MC using a frequency of 33MHz and high ^{3}He concentration at 3.7T/2MA in combination of low-power diagnostic deuterium beam injection.

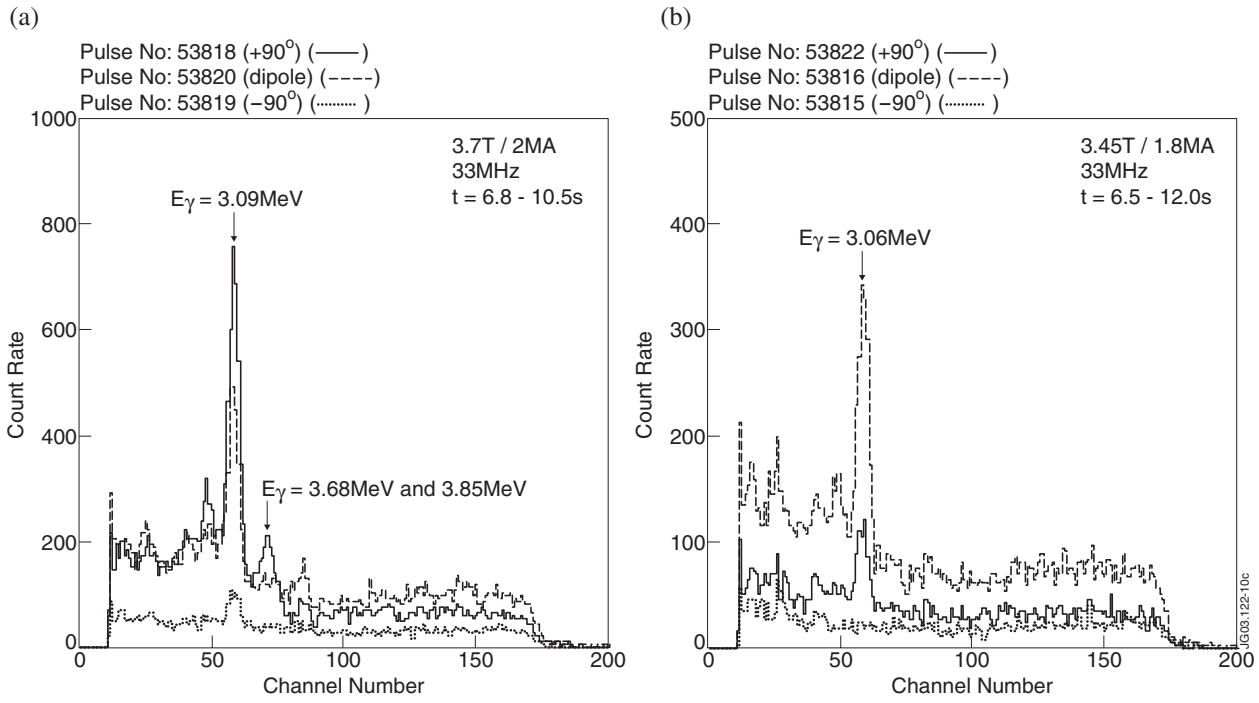

Figure 18: Gamma ray energy spectra (a) for 3.7T/2MA discharges in Fig.17 and (b) for similar discharges but at 3.45T/1.8MA. Gamma lines from reaction $^{12}C(d,p\gamma)^{13}C$ are marked.

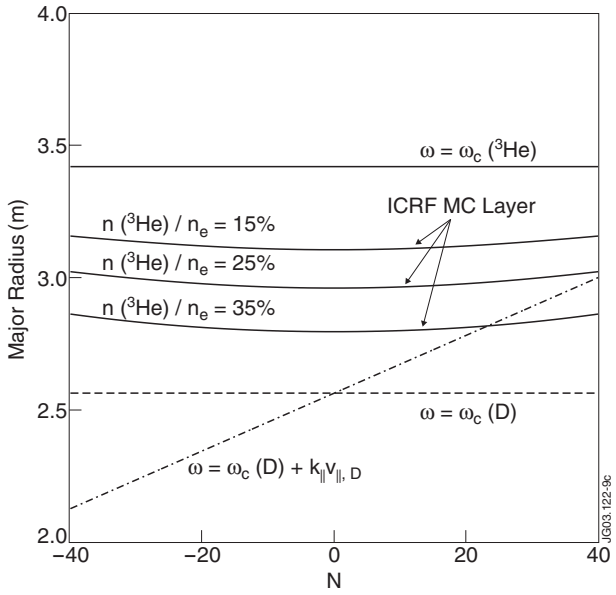

Figure 19: Schematic radial locations of the ion cyclotron resonances $\omega = \omega_c(^3He)$ and $\omega = \omega_c(D)$, the Doppler-broadened ion cyclotron resonance $\omega = n\omega_c(D) + k_{||} v_{||}$ for 135keV beam deuterons injected in the co-current direction and the ICRF MC layer $n_{||}^2 = S$ for $n(^3He)/n_e$=15, 25 and 35% as a function of the toroidal wave number. Here, we have assumed $k_{||} = N/R$, $B=B_0R_0/R$, R_0= 3 m, B_0= 3.7 T, a wave frequency of 33MHz and a plasma consisting of ^3He and D with $n_e = 3\times10^{19}$ m^{-3}.

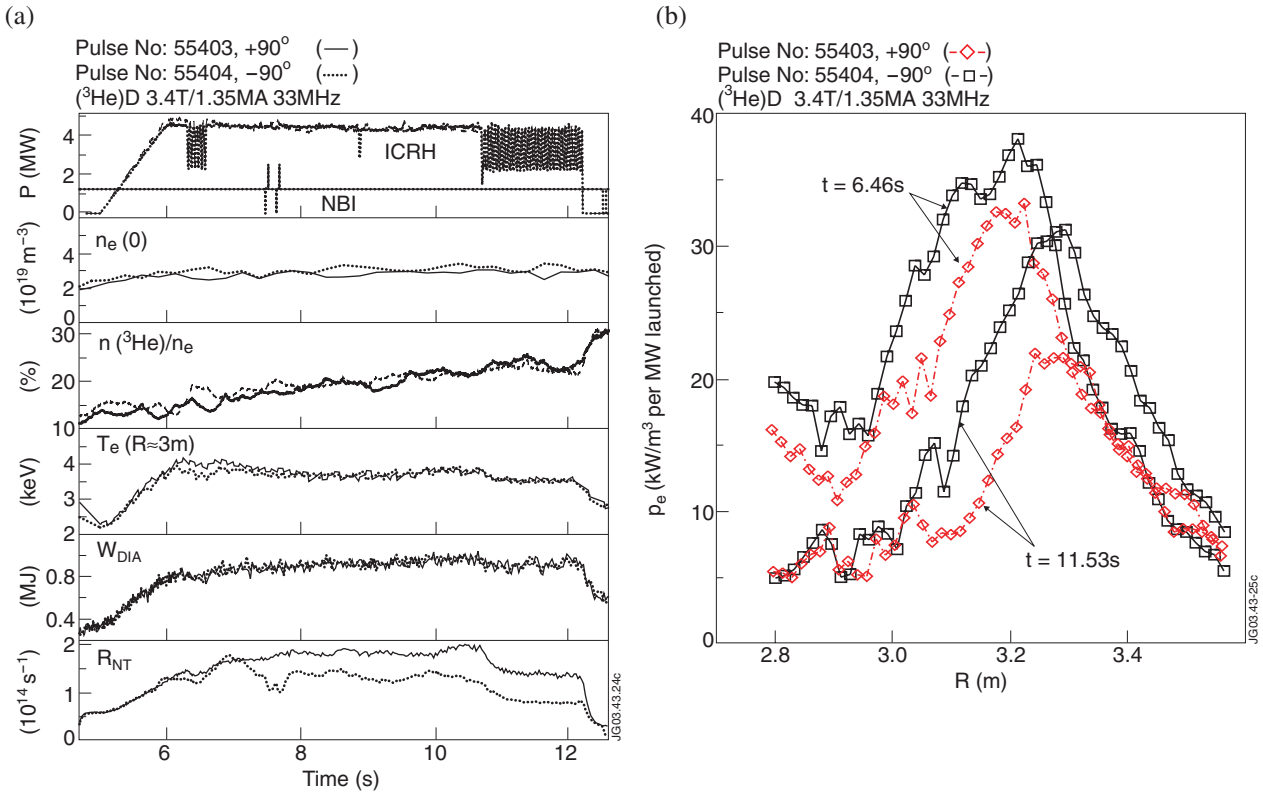

Figure 20: (a) Overview of the main plasma parameters and (b) the direct electron power deposition profiles for two discharges with $+90^o$ and -90^o phasing.

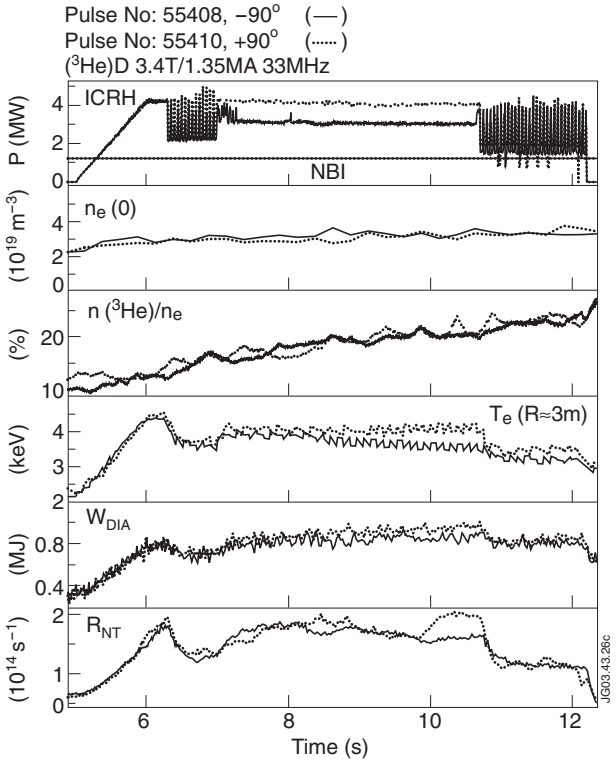

Figure 21: Neutron rate and ICRH power for discharges 55408 and 55410 with -90^o and $+90^o$ phasing, respectively.

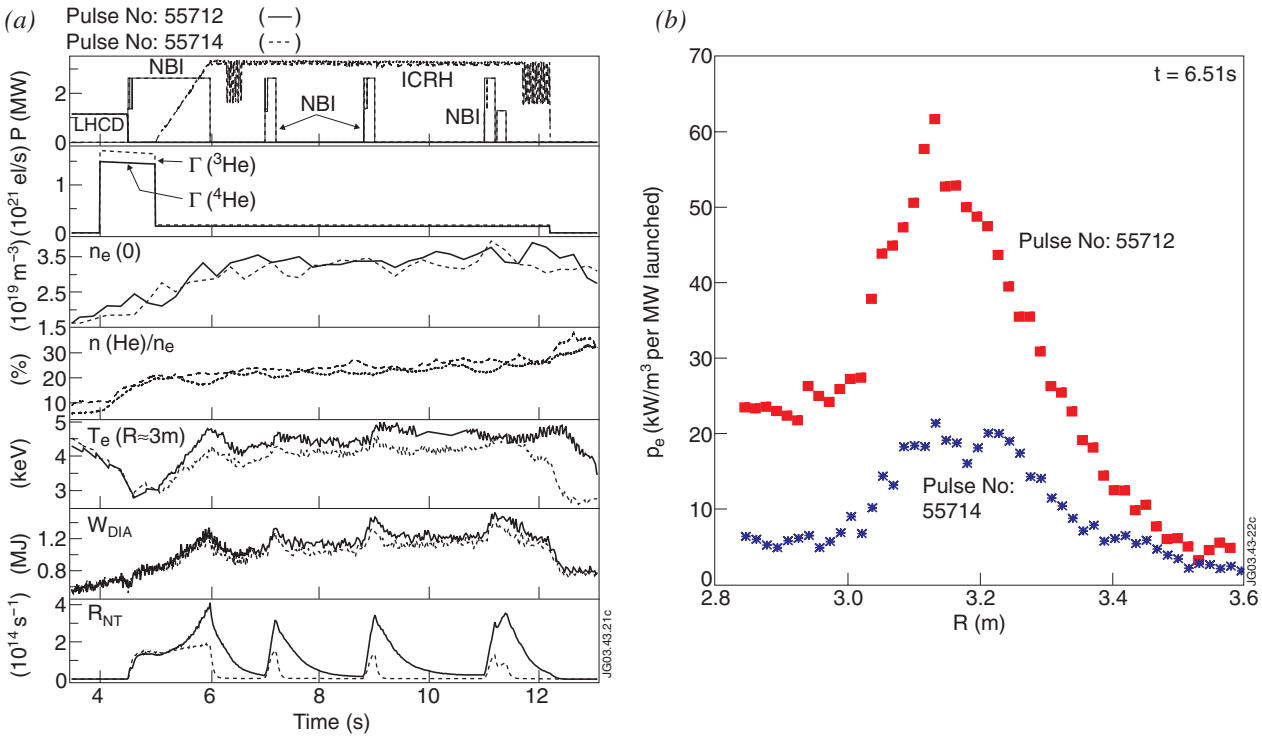

Figure 22: (a) Overview of the main plasma parameters and (b) direct electron power deposition profiles for two deuterium discharges with different ICRF schemes: ICRF MC with ^{3}He in a deuterium plasma in discharge 55712, and heating of residual ^{3}He remaining in the machine from previous discharges in discharge 55714. In discharge 55714 ^{3}He puff was replaced by ^{4}He puff to keep the plasma conditions as similar as possible to those in discharge 55712.

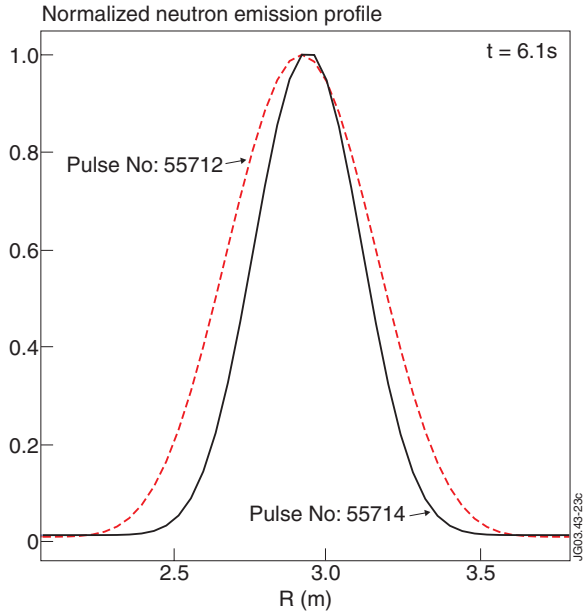

Figure 23: Neutron profiles for discharges shown in Fig. 22.